



HAL
open science

Dynamic hysteresis modelling of entangled cross-linked fibres in shear

Elsa Piollet, Dominique Poquillon, Guilhem Michon

► **To cite this version:**

Elsa Piollet, Dominique Poquillon, Guilhem Michon. Dynamic hysteresis modelling of entangled cross-linked fibres in shear. *Journal of Sound and Vibration*, 2016, 383, pp.248-264. 10.1016/j.jsv.2016.06.023 . hal-01758580

HAL Id: hal-01758580

<https://hal.science/hal-01758580>

Submitted on 4 Apr 2018

HAL is a multi-disciplinary open access archive for the deposit and dissemination of scientific research documents, whether they are published or not. The documents may come from teaching and research institutions in France or abroad, or from public or private research centers.

L'archive ouverte pluridisciplinaire **HAL**, est destinée au dépôt et à la diffusion de documents scientifiques de niveau recherche, publiés ou non, émanant des établissements d'enseignement et de recherche français ou étrangers, des laboratoires publics ou privés.





Open Archive TOULOUSE Archive Ouverte (OATAO)

OATAO is an open access repository that collects the work of some Toulouse researchers and makes it freely available over the web where possible.

This is an author's version published in : <http://oatao.univ-toulouse.fr/19782>

Official URL : <https://dx.doi.org/10.1016/j.jsv.2016.06.023>

To cite this version :

Piollet, Elsa and Poquillon, Dominique  and Michon, Guilhem 
Dynamic hysteresis modelling of entangled cross-linked fibres in shear.
(2016) Journal of Sound and Vibration, vol. 383. pp. 248-264.
ISSN 0022-460X

Any correspondence concerning this service should be sent to the repository administrator :
tech-oatao@listes-diff.inp-toulouse.fr

Dynamic hysteresis modelling of entangled cross-linked fibres in shear

Elsa Piollet ^{a,*}, Dominique Poquillon ^b, Guilhem Michon ^c

^a CREPEC, École Polytechnique, Dep. Mechanical Engineering, P.O. Box 6079 Station Centre-Ville, Montréal (Québec), Canada H3C 3A7

^b Université de Toulouse, CIRIMAT, INPT-ENSIACET, 4 allée Emile Monso, BP 44362, 31432 Toulouse, France

^c Université de Toulouse, ICA, ISAE, 10 avenue Edouard Belin, BP 54032, 31055 Toulouse, France

ABSTRACT

The objective of this paper is to characterize and model the vibration behaviour of entangled carbon fibres cross-linked with epoxy resin. The material is tested in shear, in a double lap configuration. Experimental testing is carried out for frequencies varying from 1 Hz to 80 Hz and for shear strain amplitudes ranging from $5 \cdot 10^{-4}$ to $1 \cdot 10^{-2}$. Measured shear stress-strain hysteresis loops show a nonlinear behaviour with a low frequency dependency.

The hysteresis loops are decomposed in a linear part and three nonlinear parts: a dry friction hysteresis, a stiffening term and a stiction-like overshoot term. The Generalized Dahl Model is used in conjunction with other hysteresis models to develop an appropriate description of the measured hysteresis loops, based on the three nonlinear parts. In particular, a new one-state formulation of the Bliman–Sorine model is developed. A new identification procedure is also introduced for the Dahl model, based on the so-called backbone curve. The model is shown to capture well the complex shapes of the measured hysteresis loops at all amplitudes.

ARTICLE INFO

Keywords:
Fibres
Entangled
Hysteresis
Dry friction
Dahl model

1. Introduction

Entangled materials are composed of flexible fibres with random or chosen orientations. Their properties are linked to the fibre orientation, the fibre density as well as the type of contacts between the fibres [1]. One of the interesting properties of fibrous materials is their ability to dissipate energy through friction between fibres, as shown by Poquillon [2] in static compression for example.

Recently, Mezeix [3,4] introduced a new material in which glass, aramid or carbon fibres are first entangled and then cross-linked with epoxy resin. Creating permanent links between some of the fibres increases the stiffness of the material compared to entangled fibres. This makes the entangled cross-linked material a suitable core for sandwich structures. Sandwich structures are three-layered structures in which two facesheets are separated by a core, which needs to be both lightweight and stiff enough to reach good stiffness-to-weight ratios.

So far, studies on this entangled cross-linked material have focused mainly on its process and static properties in compression, tension and bending [3–6]. A first study on the vibration properties of sandwich structures with entangled core material has shown increased damping as compared to classical core materials such as honeycomb or foams [7].

* Corresponding author.

E-mail addresses: elsa.piollet@polymtl.ca (E. Piollet), dominique.poquillon@ensiacet.fr (D. Poquillon), guilhem.michon@isae.fr (G. Michon).

However, the intrinsic behaviour of the material has not been investigated. Moreover, the vibration response was presented for one amplitude of excitation only, while fibrous materials are known to exhibit nonlinear behaviours [8]. A material study taking nonlinearity into account is thus necessary.

In order to describe a dissipative nonlinear behaviour, hysteresis models can be used. Recently, Al Majid and Dufour [9,10] introduced the Generalized Dahl Model, which allows the representation of hysteresis loops with complex shapes, relying on the description of their asymptotes. However, the expressions of the asymptotes have to be assumed, which is not straightforward for complex shapes.

This paper presents the first study of the vibration behaviour of entangled cross-linked carbon fibres to the authors' knowledge. Moreover, an original combination of existing hysteresis models is introduced, and the proposed method can be applied to a large set of physical phenomena.

The paper is organized as follows. Section 2 describes the entangled cross-linked material and the experimental set-up for shear testing. In Section 3, the measured shear stress–strain hysteresis loops are analysed and are interpreted in terms of the activated deformation mechanisms. Section 4 details the development of an adapted hysteresis model to describe the measured hysteresis loops. Section 5 presents identification procedures for the model. Finally, in Section 6 the parameters of the model are obtained and discussed.

2. Material and set-up

2.1. Material fabrication

In the present study, the entangled cross-linked material is made with carbon fibres, as they provide higher performances compared to glass or aramid fibres, albeit for a higher cost. They are widely used in aerospace applications along with epoxy resin, in particular in carbon-epoxy sandwich facesheets. The carbon fibres have a diameter of 7 μm , a Young's modulus of 240 GPa and a bulk density of 1770 kg/m^3 .

Epoxy resin is used for cross-linking because of its wide use in aeronautical applications. An injection resin with a hardener is used.

The entangled cross-linked material is made following the process introduced by Mezeix [3,4]:

- The fibres are first cut to a length of 31 mm. They are then separated and entangled in a 64 L blower room with an air flux at a 5 bar pressure applied manually. The density of the entangled material before cross-linking is 150 kg/m^3 , which represents a fibre volume fraction of 8.5 percent.
- The entangled fibres are then cross-linked by projecting epoxy resin with a paint spray gun at a 2 bar pressure. The resin droplets bond part of the contacts between the fibres. The density of epoxy resin in the final material is 30 kg/m^3 , a low density as compared to the fibre density.
- The samples are then polymerized in a mold at 70 °C during 8 h.

Fig. 1 shows a scanning electron microscope observation of the material after polymerization. As can be observed, the fibres are surrounded by air rather than a matrix: epoxy resin creates links at the contact between some fibres, while at other contacts fibres remain free to move with respect to one another.

2.2. Experimental set-up

As the entangled cross-linked material is intended to be used as a sandwich core material, its shear behaviour is of prime interest [11]. The shear set-up is presented in Fig. 2. Two samples are tested together in a double lap configuration to ensure shearing only. The set-up includes a linear vertical motor above the samples, and a load cell under the samples. The

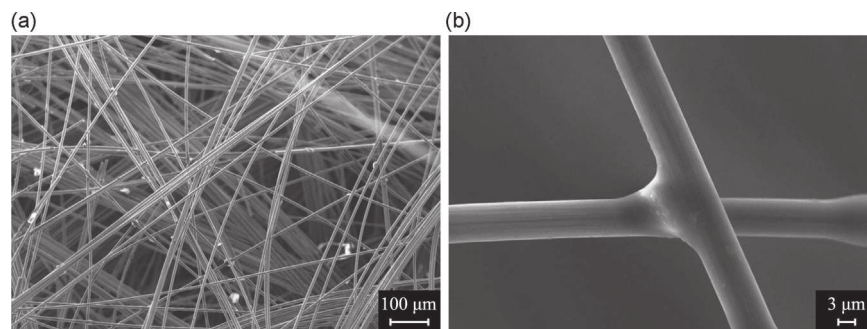


Fig. 1. Scanning electron microscope observation of entangled cross-linked carbon fibres: (a) general view showing cross-linked and free contacts and (b) zoom on a typical cross-linked contact between two carbon fibres.

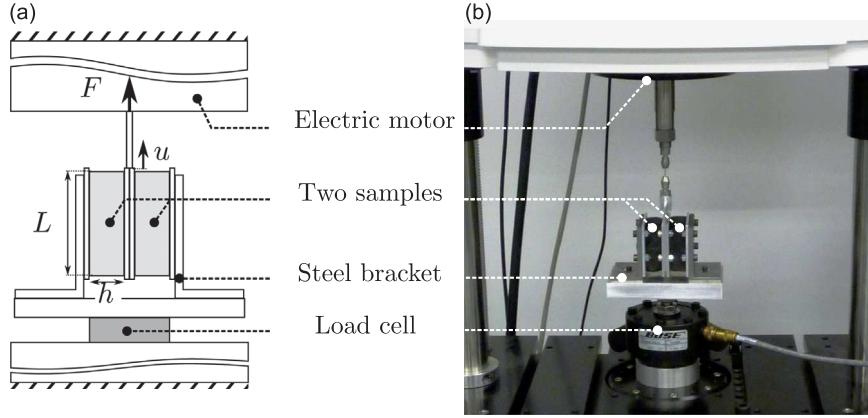


Fig. 2. Double lap shear set-up: (a) schematic principle and (b) experimental set-up.

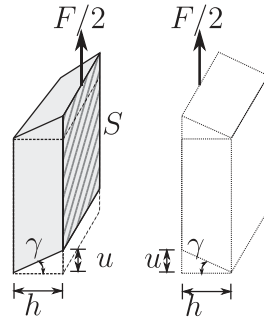


Fig. 3. Shear strain γ in each sample resulting from the applied displacement u . F is the load measured at the load cell under the samples: as the assembly is symmetrical and two identical samples tested together, it is assumed that the force applied to each sample is $F/2$.

dimensions of each sample are $h \times l \times L = 20 \text{ mm} \times 40 \text{ mm} \times 60 \text{ mm}$. The samples are glued to 3 mm thick aluminium plates on each side. Two of the plates are bolted together at the centre of the set up and linked to the vertical motor. The external plates are clamped to the load cell through two steel brackets on a thick aluminium support.

A controlled vertical displacement of amplitude u_0 and frequency f is applied to the two central plates by the electric motor:

$$u(t) = u_0 \sin(2\pi ft) \quad (1)$$

which leads to a shear strain γ in the samples, as described in Fig. 3. Assuming that shear is constant through the thickness of the samples, the engineering shear strain in small deformations is:

$$\gamma(t) = \frac{u(t)}{h} = \gamma_0 \sin(2\pi ft) \quad (2)$$

where h is the thickness of each sample.

The resulting force F at the base of the set up is measured by a load cell under the samples. The shear stress is obtained by dividing the force applied on each sample, $F/2$, by the surface through which it is applied, $S = l \times L$, resulting in the following expression:

$$\tau(t) = \frac{F(t)}{2S} \quad (3)$$

After fabrication and before making further measurements, the samples are excited at an amplitude of $\gamma_0 = 1 \cdot 10^{-2}$ and a frequency of 20 Hz. During the first cycles, the measured shear stress–strain response evolves with the number of cycles applied. The stiffness of the samples decreases, and damping increases. After around 40,000 cycles, the behaviour stabilizes. Further cycling at amplitudes under $\gamma_0 = 1 \cdot 10^{-2}$ will not modify the shear behaviour any more. Moreover, this pre-cycled behaviour is stable in time, and new series of testing after several days show the same properties for the pre-cycled samples. All measurements presented in this article are made after this pre-cycling.

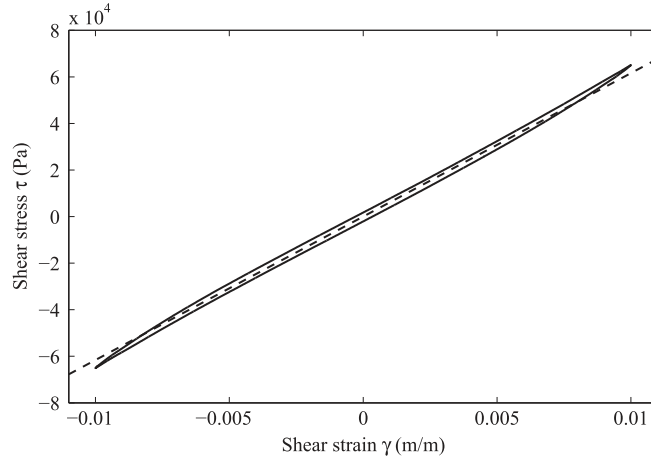


Fig. 4. Measured hysteresis loop for an amplitude $\gamma_0 = 1 \cdot 10^{-2}$ at a frequency $f = 20$ Hz. The dashed line corresponds to $\tau = G_1 \gamma$ with $G_1 = 6.16 \cdot 10^6$ Pa as identified in Section 6.

3. Measurements and first analysis

Measurements are made for an amplitude range of $\gamma_0 = 5 \cdot 10^{-4}$ to $\gamma_0 = 1 \cdot 10^{-2}$ ($u_0 = 5 \mu\text{m}$ to $u_0 = 100 \mu\text{m}$) and a frequency range of 1 Hz to 80 Hz. These ranges are limited by the set-up. The amplitude range corresponds to small deformations ($\gamma_0 \ll 1$) with a large range of variations, the minimum being 20 times smaller than the maximum. The frequency range is low compared to the frequency range of interest in structural vibrations (up to 1000 Hz or above). However it allows transitioning from the previous static studies [4,5] to vibrations studies. Testing at 1 Hz is close to static testing, while testing from 20 Hz to 80 Hz should permit highlighting vibration specific phenomena.

3.1. Linear part

Fig. 4 shows a shear stress–strain hysteresis loop measured at an amplitude of $\gamma_0 = 1 \cdot 10^{-2}$ and a frequency of 20 Hz for a set of two samples. The loop is composed of a linear part, represented by the dashed line on the figure, and a hysteresis part that carries the dissipative and nonlinear behaviour of the material. Previous studies on the behaviour of entangled fibres with and without cross-links [6] have shown that cross-links increase significantly the stiffness of the material. Thus, the linear part of the measured hysteresis can be assumed to come mainly from the carbon fibre network created by the epoxy resin bondings achieved at a large number of cross-links.

Keeping in mind this linear part, the study and following figures will focus on the hysteresis part of the stress defined as follows:

$$\tau_H = \tau - G_1 \gamma \quad (4)$$

where G_1 is a constant parameter that will be identified in Section 6.

3.2. Hysteresis loops

Fig. 5 shows τ_H plotted against γ for amplitudes ranging from $\gamma_0 = 5 \cdot 10^{-4}$ to $\gamma_0 = 1 \cdot 10^{-2}$ for the same set of two samples. As can be observed, the shapes of the hysteresis loops vary strongly with amplitude, which indicates material nonlinearity.

Fig. 6 shows the loops along with a curve linking the extrema of the loops. This curve is called the backbone curve in the fields of material study and control: in some cases, it represents the response of the tested system to an initial loading and it can be used to generate the full hysteresis curves [12–14]. This should not be confused with the backbone curve used in the description of the frequency response of nonlinear systems, even though the expression is the same.

Here, linking the extrema of the loops allows seeing the evolution of the general slope of the loops. Two lines of constant stress are also represented in Fig. 6. Both the backbone curve and the constant stress lines allow identifying two regions in the material behaviour:

- From $\gamma_0 = 5 \cdot 10^{-4}$ to $\gamma_0 = 5 \cdot 10^{-3}$, the hysteresis shape is typical of a stick-slip dry friction behaviour, as the hysteresis loops evolve between two horizontal lines of constant stress. The instantaneous slope of the backbone curve decreases at very low amplitude before becoming almost constant and equal to zero. Both the instantaneous slopes of the loops and backbone curve indicate that the material stiffness decreases with the amplitude, which is called a softening behaviour. This behaviour can be interpreted as follows. When the direction of the strain is reversed, all free contacts between the

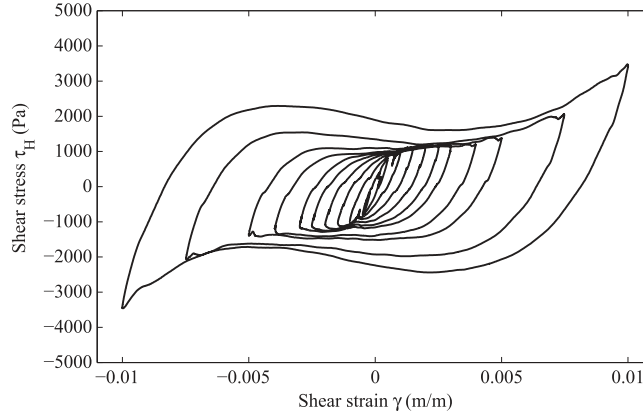


Fig. 5. Amplitude dependency of $\tau_H = \tau - G_1\gamma$ up to an amplitude $\gamma_0 = 1 \cdot 10^{-2}$ at a frequency $f = 20$ Hz. $G_1 = 6.16 \cdot 10^6$ Pa as identified in Section 6.

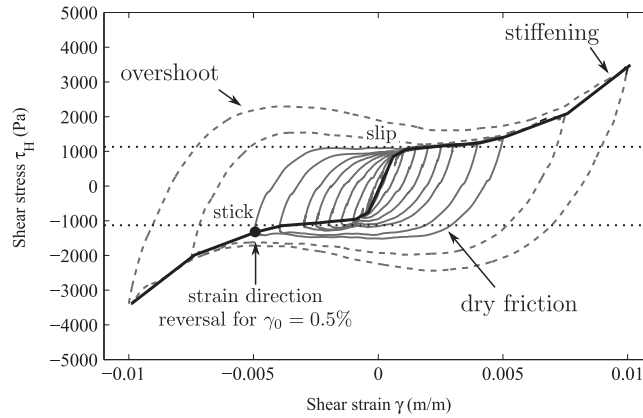


Fig. 6. Analysis of the hysteresis loops (γ, τ_H) of Fig. 5: measured loops (grey full line $\gamma_0 \leq 5 \cdot 10^{-3}$, grey dashed line $\gamma_0 > 5 \cdot 10^{-3}$), backbone curve (black full line), constant stress $\tau_H = \pm \tau_C = \pm 1.07 \cdot 10^3$ Pa as identified in Section 6 (black dotted line).

fibres are stuck, which gives extra stiffness to the fibre network. Then, as the amplitude increases, the contacts start to slip one after the other, until all non-cross-linked contacts are slipping, leading to a very low network stiffness.

- From $\gamma_0 = 5 \cdot 10^{-3}$ to $\gamma_0 = 1 \cdot 10^{-2}$, the slope of the backbone curve increases: the material exhibits a stiffening behaviour. Moreover, a clear overshoot can be observed after strain direction reversal, as the hysteresis loops exceed the horizontal asymptotes of lower amplitude behaviour. It can be assumed that when all the contacts are slipping, and all the fibres are moving, new contacts are created eventually, which leads to a stiffening of the material. An increase in the number of contacts can also lead to an increase in the material dissipation, which would explain the observed overshoot.

This physical interpretation would have to be confirmed by future fibre-level observations and modelling. Physically, the observed limit of $\gamma_0 = 5 \cdot 10^{-3}$ corresponds to $u_0 = 100 \mu\text{m}$, which is close to the average distance between the fibre cross-links of $120 \mu\text{m} \pm_{-70 \mu\text{m}}^{+140 \mu\text{m}}$ observed by Mezeix [4].

Fig. 7 shows the measured hysteresis loops for frequencies ranging from 1 Hz to 80 Hz at different amplitudes. The material exhibits a very low frequency dependency: almost no frequency dependency for low amplitudes, and a little stiffening at the highest amplitude $\gamma_0 = 1 \cdot 10^{-2}$. The observed frequency-independent behaviour confirms the hypothesis of a dry friction phenomenon.

4. Hysteresis modelling

In order to capture the material behaviour for future structural modelling, the hysteresis shapes will be described with restoring force models.

A now classical hysteresis model called the Solid Friction Model (SFM) was introduced almost fifty years ago by Dahl [15] to describe ball bearings, and was later extended to describe general friction damping phenomena [16]. With shear stress-strain

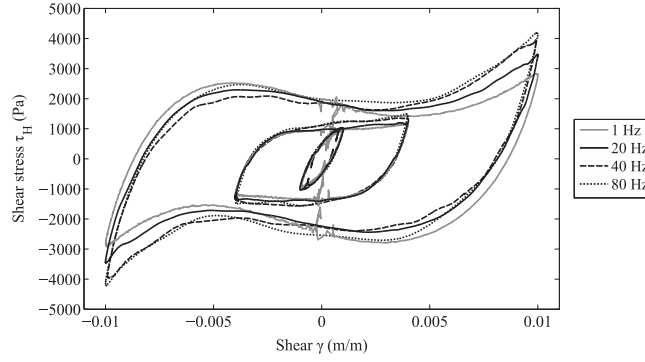


Fig. 7. Frequency dependency of $\tau_H = \tau - G_1\gamma$ for $\gamma_0 = 1 \cdot 10^{-3}$, $\gamma_0 = 4 \cdot 10^{-3}$ and $\gamma_0 = 1 \cdot 10^{-2}$. $G_1 = 6.16 \cdot 10^6$ Pa as identified in Section 6.

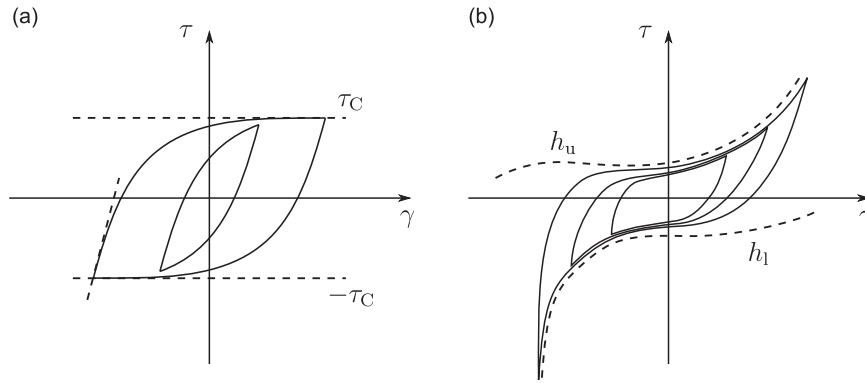


Fig. 8. Hysteresis loops as can be described by (a) Dahl's Solid Friction Model (SFM) [16] with constant asymptotes τ_C and $-\tau_C$ and (b) the Generalized Dahl Model (GDM) [9] with asymptotes h_u and h_l .

notations, the model can be written as follows:

$$\frac{d\tau}{d\gamma} = \frac{\sigma}{\tau_C} (\tau_C - \tau \operatorname{sgn}(\dot{\gamma}))^i \quad (5)$$

where σ is a constant homogeneous to a modulus, τ_C represents the asymptotic stress, sgn is the signum function, and i is a constant that controls the shape of the loop between a ductile and a brittle behaviour. The principle is that stress evolves between $-\tau_C$ and τ_C , as shown in Fig. 8(a), with the slope at $\tau = 0$ given by σ . "C" in τ_C stands for Coulomb, as the SFM yields a regularized representation of Coulomb friction.

Recently, Al Majid and Dufour [9] introduced a Generalized Dahl Model (GDM) that allows the description of complex hysteresis shapes by including general envelope curves instead of constant asymptotes, as shown in Fig. 8(b). Keeping the notations of Eq. (5), a simplified expression of the GDM can be written as follows:

$$\frac{d\tau}{d\gamma} = \frac{\sigma}{\tau_C} (h - \tau \operatorname{sgn}(\dot{\gamma}))^i \quad (6)$$

where h is an envelope function given by:

$$h = \frac{(h_u + h_l)\operatorname{sgn}(\dot{\gamma}) + (h_u - h_l)}{2} \quad (7)$$

so that h describes the upper asymptote h_u when the strain rate $\dot{\gamma}$ is positive and the lower asymptote h_l when $\dot{\gamma}$ is negative. When $h = \tau_C$, the SFM is obtained. The constant i is taken equal to 1 by most authors [10,17].

This formulation is very general and has been used to describe various damping phenomena occurring in all-metal isolators [10], elastomers [18], belt tensioners [17,19] or rubber mounts [20] for example. However, its generality also leads to challenges in its application to complex hysteresis modelling. In particular, identification relies on the assumption of h expression, which can be polynomial [17,20], but can also include exponential terms or dependency with respect to the harmonic amplitude [10] or other parameters such as temperature.

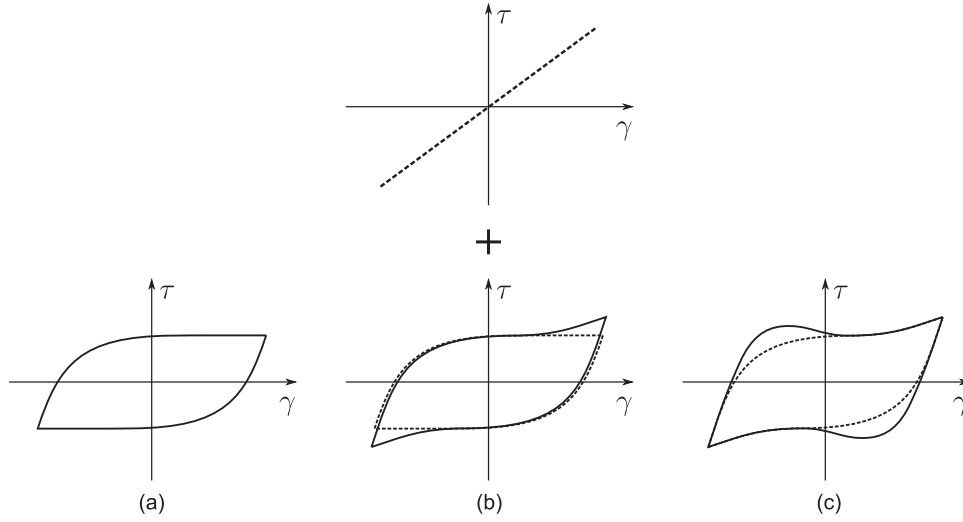


Fig. 9. Parts of the hysteresis loops used in the model decomposition: (a) dry friction hysteresis, (b) linear part and stiffening, and (c) overshoot.

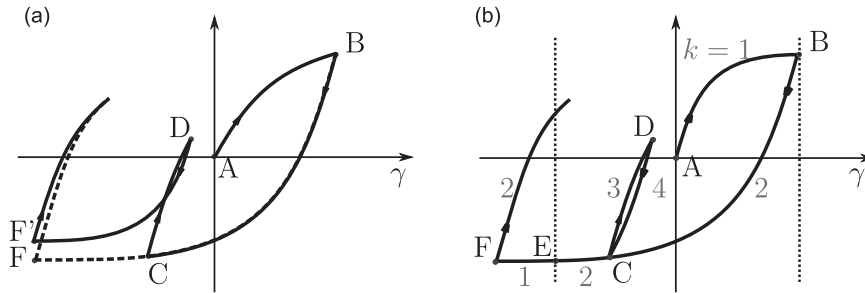


Fig. 10. Non-harmonic response to the same excitation for both Dahl models: (a) Dahl's Solid Friction Model (SFM) and (b) Dahl's Dynamic Hysteresis Model (DHM), with branch index k in grey.

4.1. A three-part hysteresis model

In the present work, the expression for h will be obtained from other hysteresis models. Based on the preliminary analysis of the measured loops in Section 3.2, the proposed model will be based on three parts, as illustrated in Fig. 9:

- Dahl's Dynamic Hysteresis Model [21] will be used to represent the classical dry-friction behaviour.
- A polynomial term will account for the linear part and the stiffening behaviour.
- A new formulation of the Bliman–Sorine model [22] will be used to include overshoot.

4.1.1. Part (a): Dahl's dynamic hysteresis model

Dahl's SFM (Eq. (5)) could be used to describe the dry friction hysteresis observed at low amplitudes (for $\gamma_0 \leq 5 \cdot 10^{-3}$). However, this model lacks nonlocal memory: its expression does not include information on the stress or strain at last change in the direction of the strain. The error arising from the lack of nonlocal memory when modelling non-harmonic response is illustrated in Fig. 10(a): F denotes the point that should be reached and F' the point that is actually reached. Moreover, even when modelling harmonic behaviour, this model leads to hysteresis loops with an initial slope depending on amplitude, which is undesirable. These limitations were addressed by Dahl in subsequent work, leading to a lesser known model, the Dynamic Hysteresis Model (DHM) [21], which principle is shown in Fig. 10(b).

The DHM is based on the Prandtl rules [21]:

- The slope of any hysteresis branch immediately after a velocity reversal is the same for all branches.
- The shape of a branch depends only on the last point of velocity reversal.
- When a branch goes through the last but one point of velocity reversal, the current loop is closed, and the branch continues as if this loop had never been formed. This is true both when closing a minor loop to return on the major loop, and when exceeding the maximum of the current major loop.

The last point corresponds to a fundamental property of hysteresis models with nonlocal memory called the wiping-out property [12,23]. This rule states that cycles with larger amplitudes wipe out the history of cycles with smaller amplitudes. Experimentally, it is indeed observed that the shape of major hysteresis loops does not depend on whether minor loops are formed or not, in a large range of fields including material plasticity [24], piezoelectric controllers [21] and friction [12]. It is also the case of the present hysteresis loops.

For stress–strain loops, the DHM links the restoring stress τ^{DHM} with the strain γ and strain rate $\dot{\gamma}$ by the following relationship:

$$\frac{d\tau^{\text{DHM}}}{d\gamma} = \sigma \left(2 - \left(\frac{\tau^{\text{DHM}} - \tau_m(k)}{\tau_c} \right) \text{sgn}(\dot{\gamma}) \right)^i \quad (8)$$

The difference between the DHM and the SFM lies in the introduction of the term $\tau_m(k)$, which accounts for the stress at last velocity reversal point, k being the index of the current branch. This allows any branch of the hysteresis to start with the same initial slope 2σ after a velocity reversal. Vector τ_m and index k are updated in the following way, as illustrated in Fig. 10(b):

- at first loading, $k=1$ and $\tau_m(1) = -\tau_c \text{sgn}(\dot{u})$ (example: branch A \rightarrow B in Fig. 10(b));
- at any strain direction reversal point, a new branch is created, k is increased by 1 and $\tau_m(k)$ takes the value of τ at the reversal point (branches B \rightarrow C, C \rightarrow D and D \rightarrow C);
- if a previous branch is crossed with $k > 2$, an internal loop is closed, the last two reversal points are “forgotten”, k is decreased by 2 (branch C \rightarrow E);
- if the current branch exceeds maximal load encountered previously, then all history is forgotten and the branch becomes a first loading branch with $k=1$ and $\tau_m(1) = -\tau_c \text{sgn}(\dot{\gamma})$ (branch E \rightarrow F).

The two last points implement the memory wipe-out described above.

In the following, parameter k is omitted for clarity.

The DHM can be seen as a particular case of the GDM presented in Eq. (6), with the following asymptote function:

$$h^{\text{DHM}}(\tau_m, \dot{\gamma}) = 2\tau_c + \tau_m \text{sgn}(\dot{\gamma}) \quad (9)$$

It must be pointed out that the actual expressions of the asymptotes do not change from the SFM to the DHM, which means that h^{DHM} is related but not equal to the expressions of the asymptotes:

$$h^{\text{DHM}}(\tau_m, \dot{\gamma}) = \underbrace{\tau_c}_{\substack{\text{asymptotes} \\ \text{(SFM)}}} + \underbrace{\tau_c + \tau_m \text{sgn}(\dot{\gamma})}_{\text{nonlocal memory}} \quad (10)$$

4.1.2. Part (b): including a polynomial term

In order to account for the linear part and the stiffening observed in the measurements, a polynomial term is included in the model:

$$\tau = \tau^{\text{DHM}} + P(\gamma) \quad (11)$$

with τ^{DHM} as defined in Eq. (8), and P a polynomial.

Again, function h of the GDM can be written for the model including a polynomial. By differentiating Eq. (11) with respect to γ :

$$\frac{d\tau}{d\gamma} = \frac{\sigma}{\tau_c} (2\tau_c - (\tau^{\text{DHM}} - \tau_m^{\text{DHM}}) \text{sgn}(\dot{\gamma})) + P'(\gamma) \quad (12)$$

and writing $\tau^{\text{DHM}} = \tau - P(\gamma)$ leads to:

$$\frac{d\tau}{d\gamma} = \frac{\sigma}{\tau_c} \left(2\tau_c + \frac{P'(\gamma)}{\sigma/\tau_c} - (\tau - P(\gamma) - (\tau_m - P(\gamma_m))) \text{sgn}(\dot{\gamma}) \right) \quad (13)$$

which corresponds to the GDM of Eq. (6) with

$$h^{\text{poly}}(\dot{\gamma}, \gamma, \gamma_m, \tau_m) = \underbrace{[\tau_c + P(\gamma) \text{sgn}(\dot{\gamma})]}_{\substack{\text{asymptotes} \\ \text{(SFM + polynomial)}}} + \underbrace{\left[\frac{P'(\gamma)}{\sigma/\tau_c} \right]}_{\text{polynomial derivative}} + \underbrace{[\tau_c + (\tau_m - P(\gamma_m)) \text{sgn}(\dot{\gamma})]}_{\text{nonlocal memory}} \quad (14)$$

The three groups of terms in Eq. (14) show that the expressions of the asymptotes must be corrected with two terms to get the expression for h : first, a term proportional to the derivative of the polynomial, and secondly, a nonlocal memory

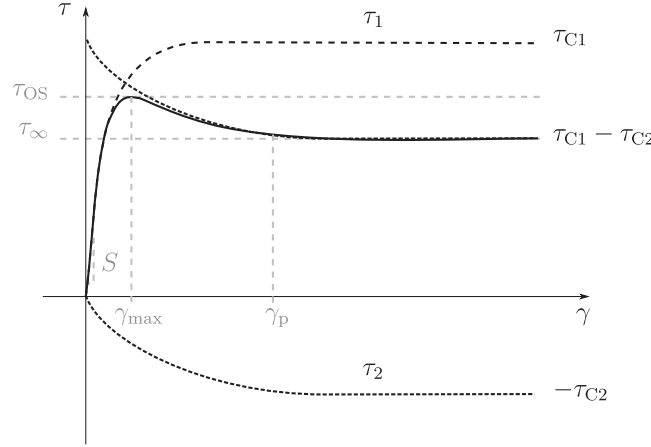


Fig. 11. The Bliman–Sorine model as the difference between two stresses τ_1 and τ_2 following the Dahl model, after [30].

term. This is an important point to note if the identification of h is made from the asymptote curves, as prescribed by Al Majid [9].

4.2. Part (c): a new formulation of the Bliman–Sorine model

Hysteresis models that take into account an overshoot after the inversion in the strain direction include the LuGre (Lund–Grenoble) friction model [25] and the Bliman–Sorine model [22]. The Bliman–Sorine model being rate independent, it is chosen here as the observed behaviour does not depend on frequency.

As illustrated in Fig. 11, the Bliman–Sorine model is defined as the sum of two Dahl models with different slope constants and asymptotic stresses of opposed signs:

$$\begin{cases} \frac{d\tau_1}{d\gamma} = \frac{\sigma_1}{\tau_{C1}} (\tau_{C1} - \tau_1 \operatorname{sgn}(\dot{\gamma})) & \tau_1(0) = 0 \quad (\text{a}) \\ \frac{d\tau_2}{d\gamma} = \frac{\sigma_2}{\tau_{C2}} (-\tau_{C2} - \tau_2 \operatorname{sgn}(\dot{\gamma})) & \tau_2(0) = 0 \quad (\text{b}) \\ \tau = \tau_1 + \tau_2 & (\text{c}) \end{cases} \quad (15)$$

where τ_1 and τ_2 represent two Dahl restoring stresses, with asymptotic stresses τ_{C1} and $-\tau_{C2}$ and initial slope σ_1/τ_{C1} and σ_2/τ_{C2} , respectively. The initial slopes are related by a factor ξ such that $\sigma_2/\tau_{C2} = \xi(\sigma_1/\tau_{C1})$ with $0 \leq \xi \leq 1$. The same model was introduced independently by Dahl some years later [26].

As discussed in Section 4.1.1, nonlocal memory is an important feature for hysteresis models to be applied to all types of excitations. The original Bliman–Sorine model is based on Dahl's original SFM [15], so it does not include nonlocal memory. The model is thus re-written here as a combination of two DHM rather than two SFM:

$$\begin{cases} \frac{d\tau_1}{d\gamma} = \frac{\sigma_1}{\tau_{C1}} (2\tau_{C1} - (\tau_1 - \tau_{m1}) \cdot \operatorname{sgn}(\dot{\gamma})) & (\text{a}) \\ \frac{d\tau_2}{d\gamma} = \frac{\xi\sigma_1}{\tau_{C1}} (-2\tau_{C2} - (\tau_2 - \tau_{m2}) \cdot \operatorname{sgn}(\dot{\gamma})) & (\text{b}) \\ \tau = \tau_1 + \tau_2 & (\text{c}) \end{cases} \quad (16)$$

where τ_{m1} and τ_{m2} are the stresses at last inversion point for τ_1 and τ_2 respectively.

Apart from the original lack of nonlocal memory, one of the criticisms against the Bliman–Sorine model is the fact that it has two states, which can lead to numerical instabilities [27]. Here, a new one-state expression is derived for $\frac{d\tau}{d\gamma}$ instead of the two state formulation. A one state formulation will be intrinsically more stable numerically than the original formulation.

Explicit expressions for τ_2 and $\frac{d\tau_2}{d\gamma}$ are obtained by first integrating and then re-deriving implicit Eq. (16b) with respect to γ :

$$\tau_2 = \tau_{m2} - 2\tau_{C2} \operatorname{sgn}(\dot{\gamma}) \left(1 - \exp\left(-\frac{\xi\sigma_1|\gamma - \gamma_m|}{\tau_{C1}}\right) \right) \quad (17)$$

$$\frac{d\tau_2}{d\gamma} = -2\xi\sigma_1 \frac{\tau_{C2}}{\tau_{C1}} \exp\left(-\frac{\xi\sigma_1|\gamma - \gamma_m|}{\tau_{C1}}\right) \quad (18)$$

where γ_m is the shear strain at last inversion point.

By deriving Eq. (16c) with respect to γ , inserting the *implicit* expression of $\frac{d\tau_1}{d\dot{\gamma}}$ Eq. (16a) and the *explicit* expression of $\frac{d\tau_2}{d\dot{\gamma}}$ Eq. (18), the following expression is obtained:

$$\frac{d\tau}{d\dot{\gamma}} = \frac{\sigma_1}{\tau_{C1}}(2\tau_{C1} - (\tau_1 - \tau_{m1}) \cdot \text{sgn}(\dot{\gamma})) - 2\xi\sigma_1\frac{\tau_{C2}}{\tau_{C1}} \exp\left(-\frac{\xi\sigma_1}{\tau_{C1}}|\gamma - \gamma_m|\right) \quad (19)$$

Then, τ_1 is replaced by $\tau - \tau_2$, τ_{m1} is replaced by $\tau_m - \tau_{m2}$, and τ_2 is replaced by its explicit expression from Eq. (17). After simplification, the final expression is:

$$\frac{d\tau}{d\dot{\gamma}} = \frac{\sigma_1}{\tau_{C1}}\left(2\tau_{C1} - 2\tau_{C2}\left(1 - (1 - \xi)\exp\left(-\frac{\xi\sigma_1}{\tau_{C1}}|\gamma - \gamma_m|\right)\right)\right) - (\tau - \tau_m) \cdot \text{sgn}(\dot{\gamma}) \quad (20)$$

This expression follows the GDM expression of Eq. (6) with an asymptotic function h^{BS} defined by:

$$h^{\text{BS}}(\dot{\gamma}, \gamma, \gamma_m, \tau_m) = 2\tau_{C1} - 2\tau_{C2}\left(1 - (1 - \xi)\exp\left(-\frac{\xi\sigma_1}{\tau_{C1}}|\gamma - \gamma_m|\right)\right) + \tau_m \cdot \text{sgn}(\dot{\gamma}) \quad (21)$$

This expression can be interpreted as follows. As γ tends to infinity, the asymptotic function tends towards $2(\tau_{C1} - \tau_{C2}) + \tau_m \cdot \text{sgn}(\dot{\gamma})$, which is the asymptotic function of a DHM with a constant asymptote $\tau_{C1} - \tau_{C2}$, as shown in Eq. (9). But immediately after a velocity reversal, the asymptotic function is equal to $2(\tau_{C1} - \xi\tau_{C2}) + \tau_m \cdot \text{sgn}(\dot{\gamma})$, which is larger, as $0 \leq \xi \leq 1$ and $\tau_{C2} < \tau_{C1}$. This higher asymptotic function allows the overshoot to occur. The asymptotic function then decreases exponentially from its value at velocity reversal to its value at infinity, which is consistent with the exponential decay observed in the Bliman–Sorine model due to the exponential behaviour of τ_2 (see Fig. 11).

4.3. Full hysteresis model

When taking into account dry friction hysteresis with nonlocal memory (part (a)), a polynomial term (part (b)) and an overshoot term (part (c)), the full expression for the model is:

$$\frac{d\tau}{d\dot{\gamma}} = \frac{\sigma_1}{\tau_{C1}}(h - \tau \text{sgn}(\dot{\gamma})) \quad (22)$$

with

$$h(\dot{\gamma}, \gamma, \gamma_m, \tau_m) = 2\tau_{C1} - 2\tau_{C2}\left(1 - (1 - \xi)\exp\left(-\frac{\xi\sigma_1}{\tau_{C1}}|\gamma - \gamma_m|\right)\right) + P(\gamma)\text{sgn}(\dot{\gamma}) + \frac{P'(\gamma)}{\sigma_1/\tau_{C1}} + (\tau_m - P(\gamma_m)) \cdot \text{sgn}(\dot{\gamma}) \quad (23)$$

As can be observed, a complex expression is obtained for h , which could not have been guessed directly from the hysteresis shape.

4.4. Model parameters and physical considerations

The general model is now adapted to the measured hysteresis loops in order to clarify the constant parameters that need to be identified for future simulations.

Polynomial: A simple polynomial expression is chosen to include the linear part of the loops as well as the observed stiffening behaviour:

$$P(\gamma) = G_1\gamma + G_3\gamma^3 \quad (24)$$

where G_1 and G_3 are constant coefficients.

Overshoot: The effect of part (c) of the model should only be to add an overshoot to the dry friction loops of part (a). In particular, both the asymptotic stress and initial slope should remain unchanged when adding the overshoot. To this end, τ_{C1} , τ_{C2} and σ_1 should be expressed with respect to the DHM parameters:

- By definition of the Bliman–Sorine model, the final asymptote of the model is obtained by the difference between the two asymptotes (see Eqs. (16a)–(16c) and Fig. 11). As τ_c is the asymptotic stress for the DHM, the relationship is the following:

$$\tau_{C1} - \tau_{C2} = \tau_c \quad (25)$$

- Writing the initial slopes for both models from Eqs. (8) and (20) allows expressing σ_1 as a function of σ :

$$\left.\frac{d\tau}{d\dot{\gamma}}\right|_{\gamma=\gamma_m} = \frac{2\sigma_1}{\tau_{C1}}(\tau_{C1} - \xi\tau_{C2}) = 2\sigma \quad (26)$$

which leads to:

$$\sigma_1 = \sigma \frac{\tau_{C1}}{\tau_{C1} - \xi\tau_{C2}} \quad (27)$$

Another element to take into account is the fact that the overshoot only appears at higher amplitudes in the experimental loops. In order to capture this behaviour, τ_{C2} should depend on the amplitude. The type of amplitude dependency has to be decided based on experimental observations. Both overshoot and stiffening were interpreted as a consequence of an increase in the number of contacts, as discussed in Section 3.2. In particular, the higher the amplitude, the more visible the stiffening, and the higher the overshoot. Thus, an hypothesis is made that the overshoot and the stiffening phenomenon are related. This is implemented by making τ_{C2} proportional to the stiffening term at reversal point:

$$\tau_{C2}(\gamma_m) = \alpha G_3 \gamma_m^3 \quad (28)$$

where α is a constant to be determined.

From Eqs. (25), (27) and (28), it can be observed that τ_{C1} and σ_1 will also depend on the amplitude:

$$\tau_{C1}(\gamma_m) = \tau_C + \tau_{C2}(\gamma_m) \quad (29)$$

$$\sigma_1(\gamma_m) = \sigma \frac{\tau_C + \tau_{C2}(\gamma_m)}{\tau_C + \tau_{C2}(\gamma_m)(1 - \xi)} \quad (30)$$

Finally, the constant parameters to identify for the full model are the following:

- the two DHM parameters τ_C and σ ;
- two polynomial parameters: the “linear shear modulus” G_1 and the coefficient for the cubic term G_3 ;
- the two parameters for the overshoot model ξ and $\alpha = \tau_{C2}(\gamma_m)/G_3\gamma_m^3$.

All the other parameters for the overshoot model, $\tau_{C2}(\gamma_m)$, $\tau_{C1}(\gamma_m)$ and $\sigma_1(\gamma_m)$ can then be expressed from the previous parameters.

5. Identification methods

In order to use the GDM, parameters are generally identified from the asymptotes of the hysteresis loops and their inner area [9,17]. However, this leads to two main issues:

- First, as was shown in Sections 4.1.1 and 4.1.2, the function h is related but not equal to the equation of the asymptotes, and identification must be carried out carefully by including correction terms.
- Second, for complex shapes as encountered here, it is not trivial to obtain the asymptotes, as by definition the loops are not superposed or even close to the asymptotes except for high levels of deformation.

Here, the identification method relies on the decomposition of the model in three parts. In particular, a new identification method is developed for the DHM and extended to the addition of any polynomial term.

5.1. Identification of the DHM parameters

Instead of relying on the asymptote, the proposed identification method for the DHM relies on the backbone curve of the hysteresis loops (see Section 3.2 and Fig. 12).

Eq. (8) is integrated to obtain the explicit expression of the stress for the DHM:

$$\tau^{\text{DHM}} = \tau_m + 2\tau_C \left(1 - e^{-\frac{\sigma}{\tau_C} |\gamma - \gamma_m|} \right) \text{sgn}(\dot{\gamma}) \quad (31)$$

Under a harmonic motion of amplitude γ_0 , the loops are comprised between a minimum point $(\gamma_{\min}, \tau_{\min})$ and a maximum point $(\gamma_{\max}, \tau_{\max})$, with $\gamma_{\max} = \gamma_0$ and $\gamma_{\min} = -\gamma_0$. The minimum and maximum points are the only reversal

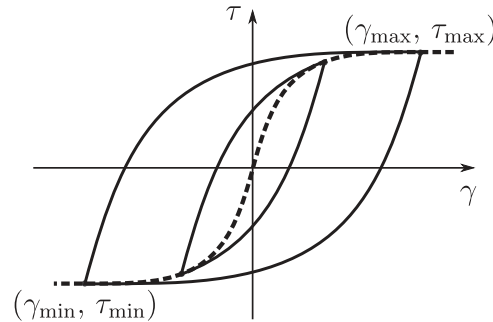


Fig. 12. Schematic representation of hysteresis loops (full line) with corresponding backbone curve (dashed line).

points, and thus:

$$\begin{cases} (\tau_m, \gamma_m) = (\tau_{\min}, \gamma_{\min}) & \text{if } \text{sgn}(\dot{\gamma}) > 0 \\ (\tau_m, \gamma_m) = (\tau_{\max}, \gamma_{\max}) & \text{if } \text{sgn}(\dot{\gamma}) < 0 \end{cases} \quad (32)$$

As the DHM is symmetrical and the motion is harmonic, the maximum and minimum are related as follows:

$$(\gamma_{\min}, \tau_{\min}) = (-\gamma_{\max}, -\tau_{\max}) \quad (33)$$

Moreover, τ_{\max} is reached from τ_{\min} when $\text{sgn}(\dot{\gamma}) > 0$, and τ_{\min} is reached from τ_{\max} when $\text{sgn}(\dot{\gamma}) < 0$. Inserting Eqs. (33) and (32) in Eq. (31), the following expression for the backbone curve is obtained:

$$\tau_m = f_{\text{bb}}(\gamma_m) \quad (34)$$

$$f_{\text{bb}}(\gamma) = \tau_c \left(1 - e^{-2\frac{\sigma_c}{\tau_c}|\gamma|} \right) \text{sgn}(\gamma) \quad (35)$$

with $(\gamma_m, \tau_m) = (\gamma_{\min}, \tau_{\min})$ or $(\gamma_{\max}, \tau_{\max})$. This expression contains all the parameters of the DHM, and allows a simple identification from the minimum and maximum points of experimental loops measured at different amplitudes.

It can be noted that Eq. (31) can be obtained from Eq. (35) by replacing τ_m by $(\tau - \tau_m)/2$ and γ_m by $(\gamma - \gamma_m)/2$. The DHM is actually a specific case of the Masing rules [12], with an exponential backbone curve.

5.2. Extension to the DHM with a polynomial term

The backbone curve identification method presented in the previous section allows the inclusion of any polynomial term in the identification process without extra effort. Indeed, at a given loop extremum, adding the polynomial only shifts the stress by the polynomial value at this extremum: $\tau'_m = \tau_m + P(\gamma_m)$. The expression of the backbone curve becomes:

$$f_{\text{bb}}(\gamma) = \tau_c \left(1 - e^{-2\frac{\sigma_c}{\tau_c}|\gamma|} \right) \text{sgn}(\gamma) + P(\gamma) \quad (36)$$

5.3. Identification method for the overshoot

The overshoot model parameters ξ and α can be identified in two different ways. As both Bliman and Sorine [22] and Dahl [26] proposed the same overshoot model separately, they also proposed their own identification procedures. Fig. 11 shows the five measurable values that are used by one or the other identification method:

- τ_{∞} is the stress when strain approaches infinity: $\tau_{\infty} = \lim_{\gamma \rightarrow \infty} \tau = \tau_{c1} - \tau_{c2}$;
- τ_{OS} is the maximal stress reached at overshoot;
- γ_{OS} is the shear strain for which τ_{OS} is reached;
- S is the initial slope: $S = \left. \frac{d\tau}{d\gamma} \right|_{\gamma=0}$;
- γ_p is the strain for which the stress is within 5 percent of τ_{∞} .

Dahl [26] bases his identification method on S , τ_{OS} , γ_{OS} and τ_{∞} , while Bliman and Sorine [22] base theirs on τ_{OS} , γ_{OS} , τ_{∞} and γ_p . In the present case, as the initial slope is an important characteristic of the hysteresis loops related to the network architecture, Dahl's identification procedure will be preferred. Moreover, parameter γ_p can be hard to identify from experimental loops where the decrease to the asymptote may not be a clean exponential decrease. The corresponding equations for Dahl's identification are presented in Appendix A.

6. Parameter identification and interpretation

6.1. Backbone curve identification of parts (a) and (b)

Parts (a) (Dahl's DHM) and (b) (polynomial term) of the model are first identified using the backbone curve method. The experimental backbone curve is defined from the extrema of the measured loops for all ten amplitudes from $\gamma_0 = 5 \cdot 10^{-4}$ to $\gamma_0 = 1 \cdot 10^{-2}$, for the hysteresis loops measured at 20 Hz, as shown in Fig. 13. The extrema are centred, with the hypothesis that in this shear test the loops should be symmetrical. From Eqs. (24) and (36), the backbone curve expression is:

$$f_{\text{bb}}(\gamma) = \tau_c \left(1 - e^{-2\frac{\sigma_c}{\tau_c}|\gamma|} \right) \text{sgn}(\gamma) + G_1\gamma + G_3\gamma^3 \quad (37)$$

The nonlinear least-square method is used to identify the parameters of this function from the ten experimental points, using MATLAB *Curve Fitting Toolbox*. Fig. 13 shows a comparison between measured and simulated loops for parts (a) and (b) of the model, representing only the hysteresis without linear part $\tau - G_1\gamma$ for legibility. Up to $\gamma_0 = 5 \cdot 10^{-4}$, the hysteresis

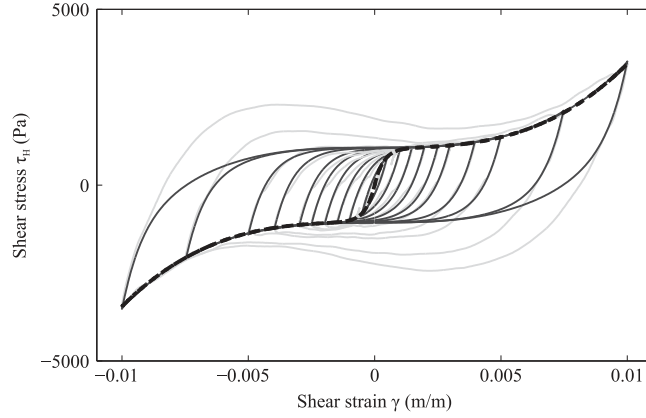


Fig. 13. Measured hysteresis loops for the first set of samples at 20 Hz (light grey full line), and corresponding backbone curve (black dashed line) and simulated hysteresis loops with parts (a) and (b) of the model $\alpha = 0$ and $\xi = 0$ (dark grey full line). The removed linear modulus value is $G_1 = 6.16 \cdot 10^6$ Pa.

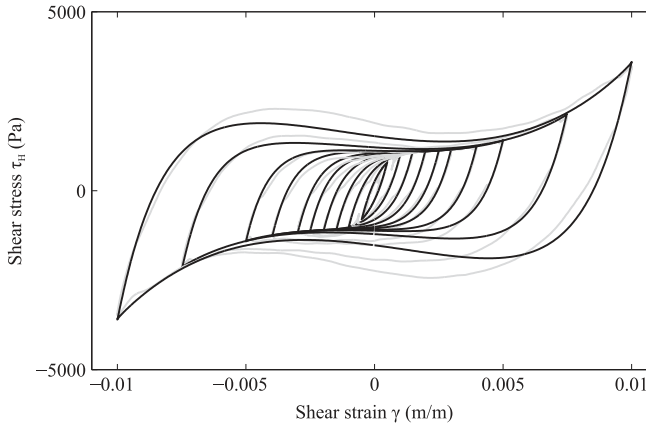


Fig. 14. Measured hysteresis loops for the first set of samples at 20 Hz (light grey line) and simulated hysteresis loops with the full model including overshoot (dark grey line). The removed linear modulus value is $G_1 = 6.16 \cdot 10^6$ Pa.

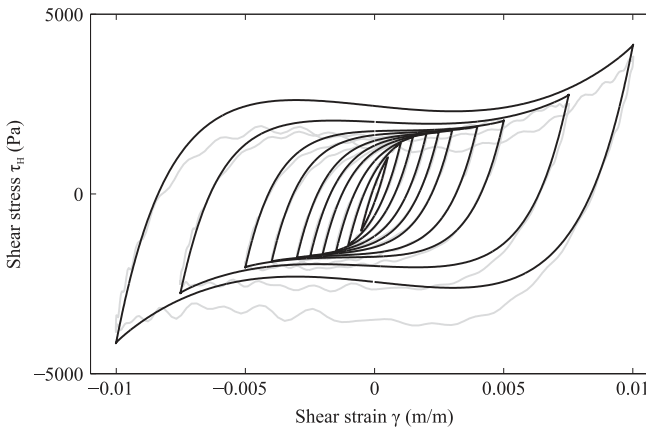


Fig. 15. Measured hysteresis loops for the second set of samples at 20 Hz (light grey line), and simulated hysteresis loops with the full model including overshoot (dark grey full line). The removed linear modulus value is $G_1 = 5.91 \cdot 10^6$ Pa.

loops are well represented. For higher amplitudes, the overshoot phenomenon is clearly visible, which confirms the need for the third part of the model.

The parameters found for this set of samples at 20 Hz are:

$$\begin{aligned} \tau_c &= 1.07 \cdot 10^3 \text{ Pa} & \sigma &= 1.49 \cdot 10^6 \text{ Pa} \\ G_1 &= 6.16 \cdot 10^6 \text{ Pa} & G_3 &= 2.38 \cdot 10^9 \text{ Pa} \end{aligned} \quad (38)$$

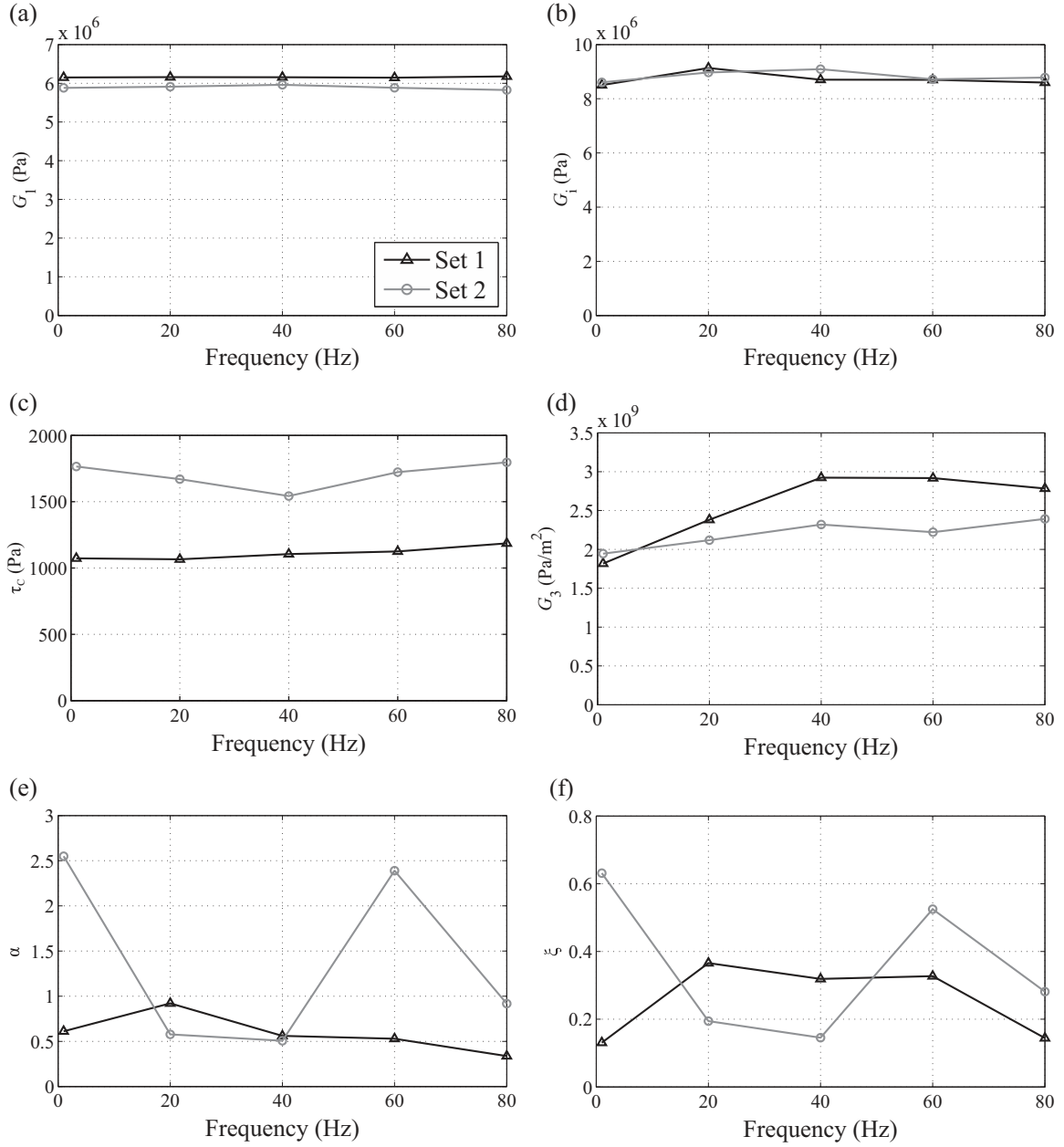


Fig. 16. Parameters for the two sets of samples: (a) asymptotic modulus, G_1 , (b) initial modulus G_i , (c) asymptotic stress τ_c , (d) cubic coefficient G_3 , (e) overshoot parameter α and (f) overshoot parameter ξ . Parameters are identified on the backbone curve for ten amplitudes ranging from $\gamma_0 = 5 \cdot 10^{-4}$ to $\gamma_0 = 1 \cdot 10^{-2}$ for parameters G_1 , G_i , τ_c and G_3 and on the full loop at one amplitude $\gamma_0 = 1 \cdot 10^{-2}$ for overshoot parameters α and ξ .

A new parameter is introduced: $G_i = G_1 + 2\sigma$. This parameter corresponds to the initial slope of the hysteresis loops, and thus to the modulus at very low amplitudes. From the values identified, $G_i = 9.14 \cdot 10^6$ Pa. On the other hand, G_1 corresponds to the asymptotic modulus, which is the modulus that would be reached at high amplitudes if there were no cubic term. Thus, the slope of the loop varies from G_i to G_1 as the amplitude increases from a reversal point.

6.2. Identification of part (c) model parameters

The overshoot parameters ξ and α are now identified to be able to use the full model of Eqs. (22) and (23). Identification is carried out on the hysteresis loop of highest amplitude, $\gamma_0 = 1 \cdot 10^{-2}$. Parameters S , τ_{OS} , γ_{OS} and τ_∞ (Fig. 11) are identified successively on the superior ($\dot{\gamma} > 0$) and inferior ($\dot{\gamma} < 0$) branches of the hysteresis loop. The obtained parameters are then

averaged to compensate for the asymmetry that could appear during measurement. Dahl's method (Appendix A) gives ξ and $\tau_{C2}(\gamma_m)$, from which $\alpha = \tau_{C2}(\gamma_m)/G_3\gamma_m^3$ is deduced.

The parameters found are:

$$\alpha = 0.92 \quad \xi = 0.37 \quad (39)$$

Fig. 14 shows the same experimental loops as Fig. 13, compared with the full model. While there are still discrepancies between the model and experimental loops, the general behaviour is very well represented by the full model.

6.3. Variability and frequency dependency

A second set of samples was tested under the same conditions as the first set. Then, the identification procedure was applied to obtain the corresponding parameters for the model. Fig. 15 shows the measured loops at 20 Hz as well as the simulated loops. Note that the linear modulus, removed from all figures, is slightly lower for the second set of samples, with $G_1 = 5.91 \cdot 10^6$ Pa. Another difference that can be observed directly from the loops is that the samples of the second set exhibit higher energy dissipation: the loops are more open than for the first set of samples.

Fig. 16 shows a comparison between the identified parameters for both sets and for frequencies ranging from 1 Hz to 80 Hz.

It can be seen that the obtained values for the asymptotic and initial moduli G_1 and G_i are very close for both sets and have a very low frequency dependency, with slightly lower values for set 2. As the modulus evolves between G_i and G_1 , it evolves roughly between 9 MPa and 6 MPa. While there has been no previous study on the shear behaviour of the material, a finite element analysis by Mezeix [28] indicated a shear modulus of 10 MPa. The order of magnitude is consistent with the present work.

Asymptotic stress τ_c also has a low frequency dependency, but with a large difference between the two sets. This is consistent with the fact that the loops measured for set 2 are more open than those measured for set 1. Parameter G_3 exhibits first a low difference between samples, which increases with frequency. This parameter is the only parameter of parts (a) and (b) that exhibits some frequency dependency: the parameter increases, which is consistent with the preliminary analysis in Section 3.2 and with observations made by Janghorban on entangled fibres [29].

Finally, regarding parameters of the overshoot model (part (c)), a larger variation is observed both between samples and with frequency. This is due to the fact that the overshoot region in the loops is more subject to noise. The identification was not as efficient as for the other parameters, which indicates the need for a more robust identification process for this part. However, the obtained values still give the order of magnitude of those parameters.

This comparison between two sets of samples confirms the general behaviour observed for the first set of samples. The samples exhibit a low variability in modulus, but a higher variability in energy dissipation and stiffening behaviour. It is worth remembering that the samples are currently made manually. The good repeatability in modulus is a positive information, while the variability in energy dissipation indicates that more work is needed to understand and control better this fundamental property. The low frequency dependency of the material behaviour was also confirmed by parameter identification.

7. Conclusions

The shear behaviour of entangled cross-linked carbon fibres was studied at frequencies from 1 Hz to 80 Hz. Experimental testing of the material for amplitudes up to $\gamma_0 = 1 \cdot 10^{-2}$ showed a nonlinear behaviour with very low frequency dependency. The analysis of the measured shear stress–strain hysteresis loops lead to a decomposition of the behaviour between a linear part and three nonlinear parts: a dry friction hysteresis (part (a)), a stiffening (part (b)) and an overshoot (part (c)), the two last parts appearing only at amplitudes higher than $\gamma_0 = 5 \cdot 10^{-3}$. The linear part was attributed to the stiffness of the cross-linked contacts. Part (a) was attributed to fibres slipping against each other at free contacts. Parts (b) and (c) were assumed to come from the creation of new contacts between fibres at higher deformation amplitudes.

The hysteresis loops were modelled using Al Majid and Dufour's Generalized Dahl Model. Instead of assuming the expression of the asymptote function for this model, the three nonlinear parts of the behaviour were modelled separately before combining them. Dry friction was modelled using Dahl's lesser known Dynamic Hysteresis Model, and stiffening was included with a polynomial term. It was shown that the asymptote function in the Generalized Dahl Model is in fact related to but not equal to the actual asymptotes' equations. A new one-state formulation for the Bliman–Sorine overshoot model was developed.

A new identification method was introduced for the Dynamic Hysteresis Model, relying on the backbone curve, and was extended to the addition of a polynomial term. The identification of the model parameters lead to a good capture of the hysteresis loops, showing the relevance of the developed model. Comparison between two sets of samples showed similar behaviours, but with some variability in the energy dissipation that could be analysed in further studies on the fabrication process of the material.

While the proposed combination of hysteresis models was applied to entangled cross-linked fibres in the present work, it could be used to model a large set of phenomena including friction, elasto-plasticity, stiffening, softening or stiction among

others. Other shapes could be modelled with the same model principle: asymmetrical loops can be achieved by using asymmetrical polynomials, or by defining different asymptotic functions for the upper and lower asymptotes.

Ongoing work will analyse the effect of the observed material behaviour on the vibratory response of a structure. The material model will be used in the analysis of both harmonic and transient nonlinear responses.

Acknowledgements

This study was carried out during the first author's PhD work at Institut Supérieur de l'Aéronautique et de l'Espace (ISAE) in Toulouse, France. Région Midi Pyrénées and Université de Toulouse are gratefully acknowledged for their financial support.

Appendix A. Dahl's identification method for the overshoot model

The following parameters are defined from the parameters of Fig. 11:

$$d = \frac{\tau_{C2}}{\tau_{\infty}} = \frac{\tau_{C2}}{\tau_{C1} - \tau_{C2}} \quad (\text{A.1})$$

$$c = \frac{1}{\xi} \quad (\text{A.2})$$

$$\text{OS} = \frac{\tau_{\text{OS}}}{\tau_{\infty}} \quad (\text{A.3})$$

$$K = S \frac{\gamma_{\text{OS}}}{\tau_{\infty}} \quad (\text{A.4})$$

In order to obtain c and d , the following system must be solved:

$$\begin{cases} \text{OS} = (d+1)(c-1)\exp\left(-\frac{c}{c-1}\ln\left(c+\frac{c}{d}\right)\right) \\ K = \frac{c+cd-d}{c-1}\ln\left(c+\frac{c}{d}\right) \end{cases} \quad (\text{A.5})$$

From c and d , the model parameters are obtained through the following relationships:

$$\begin{cases} \tau_{C2} = d \times \tau_{\infty} \\ \tau_{C1} = \tau_{\infty} + \tau_{C2} \\ \xi = \frac{1}{c} \\ \sigma = \frac{c\tau_{C1}}{c\tau_{C1} - \tau_{C2}} S \end{cases} \quad (\text{A.6})$$

References

- [1] C. Barbier, R. Dendievel, D. Rodney, Role of friction in the mechanics of nonbonded fibrous materials, *Physical Review E* 80 (1) (2009) 016115–1–5.
- [2] D. Poquillon, B. Viguiet, E. Andrieu, Experimental data about mechanical behaviour during compression tests for various matted fibres, *Journal of Materials Science* 40 (2005) 5963–5970.
- [3] L. Mezeix, C. Bouvet, J. Huez, D. Poquillon, Mechanical behavior of entangled fibers and entangled cross-linked fibers during compression, *Journal of Materials Science* 44 (14) (2009) 3652–3661.
- [4] L. Mezeix, D. Poquillon, C. Bouvet, Entangled cross-linked fibres for an application as core material for sandwich structures part I: *experimental investigation*, *Applied Composite Materials* (2015) 1–16.
- [5] L. Mezeix, D. Poquillon, C. Bouvet, Entangled cross-linked fibres for an application as core material for sandwich structures – part II: *analytical model*, *Applied Composite Materials* (2015) 1–14.
- [6] J.-P. Masse, D. Poquillon, Mechanical behavior of entangled materials with or without cross-linked fibers, *Scripta Materialia* 68 (2013) 39–43.
- [7] A. Shahdin, L. Mezeix, C. Bouvet, J. Morlier, Y. Gourinat, Fabrication and mechanical testing of glass fiber entangled sandwich beams: *a comparison with honeycomb and foam sandwich beams*, *Composite Structures* 90 (2009) 404–412.
- [8] T. Pritz, Frequency dependance of frame dynamic characteristics of mineral and glass wool materials, *Journal of Sound and Vibration* 106 (1986) 161–169.
- [9] A. Al Majid, R. Dufour, Formulation of a hysteretic restoring force model. Application to vibration isolation, *Nonlinear Dynamics* 27 (2002) 69–85.
- [10] A. Al Majid, R. Dufour, Harmonic response of a structure mounted on an isolator modelled with a hysteretic operator: *experiments and predictions*, *Journal of Sound and Vibration* 277 (2004) 391–403.
- [11] D.J. Mead, A comparison of some equations for the flexural vibration of damped sandwich beams, *Journal of Sound and Vibration* 83 (1982) 363–377.
- [12] F. Al-Bender, W. Symens, J. Swevers, H. Van Brussel, Theoretical analysis of the dynamic behavior of hysteresis elements in mechanical systems, *Journal of Non-Linear Mechanics* 39 (2004) 1721–1735.
- [13] G. Muravskii, Application of hysteresis functions in vibration problems, *Journal of Sound and Vibration* 319 (2009) 476–490.
- [14] M. Ismail, F. Ikhouane, J. Rodellar, The hysteresis Bouc–Wen model, a survey, *Archives of Computational Methods in Engineering* 16 (2009) 161–188.
- [15] P.R. Dahl, A Solid Friction Model, Technical Report, The Aerospace Corporation, May 1968.

- [16] P.R. Dahl, Solid friction damping of mechanical vibrations, *AIAA Journal* 14 (12) (1976) 1675–1682.
- [17] G. Michon, L. Manin, R. Dufour, Hysteretic behavior of a belt tensioner: modeling and experimental investigation, *Journal of Vibration and Control* 11 (9) (2005) 1147–1158.
- [18] P. Saad, A. Al Majid, F. Thouverez, R. Dufour, Equivalent rheological and restoring force models for predicting the harmonic response of elastomer specimens, *Journal of Sound and Vibration* 290 (2006) 619–639.
- [19] J. Bastien, G. Michon, L. Manin, R. Dufour, An analysis of the modified Dahl and Masing models: application to a belt tensioner, *Journal of Sound and Vibration* 302 (4–5) (2007) 841–864, <http://dx.doi.org/10.1016/j.jsv.2006.12.013>.
- [20] B. Thomas, L. Manin, P. Goge, R. Dufour, A rubber mount model, Application to automotive equipment suspension, *ISMA2010 International Conference on Noise and Vibration Engineering*, Leuven, Belgium, 2010, 2010.
- [21] P.R. Dahl, R. Wilder, Math model of hysteresis in piezo-electric actuators for precision pointing systems, *Guidance and Control*, 1985, pp. 61–88.
- [22] P.-A. Bliman, M. Sorine, Easy-to-use realistic dry friction models for automatic control, *Proceedings of 3rd European Control Conference*, 1995, pp. 3788–3794.
- [23] A. Visintin, Chapter 1 – Mathematical models of hysteresis, in: G. Bertotti, I.D. Mayergoyz (Eds.), *The Science of Hysteresis*, Academic Press, Oxford, 2006, pp. 1–123. ISBN 9780124808744, <http://dx.doi.org/10.1016/B978-012480874-4/50004-X>.
- [24] P. Jayakumar, Modeling and Identification in Structural Dynamics, PhD Thesis, California Institute of Technology, 1987.
- [25] C. Canudas de Wit, H. Olsson, K.J. Astrom, P. Lischinsky, A new model for control of systems with friction, *IEEE Transactions on Automatic Control* 40 (1995) 419–425.
- [26] P.R. Dahl, Dynamic hysteresis model application to stiction type problems, *Guidance and Control* 2001, 2001, pp. 95–111.
- [27] M. Gäfvert, Comparisons of two dynamic friction models, *Proceedings of the 1997 IEEE International Conference on Control Applications*, 1997, pp. 386–391.
- [28] L. Mezeix, Développement de matériaux d'âme pour structures sandwich à base de fibres enchevêtrées [Core Material Development for Sandwich Structures with Entangled Fibres], PhD Thesis, Université Paul Sabatier, Toulouse, 2010.
- [29] A. Janghorban, D. Poquillon, B. Viguiier, E. Andrieu, Compression de fibres enchevêtrées modèles [Compression of Calibrated Entangled Fibres], *Matériaux 2006*, Dijon, France, 2006.
- [30] B. Borsotto, Modélisation, identification et commande d'un organe de friction. Application au contrôle d'un système d'embrayage et au filtrage d'acyclismes par glissement piloté [Modelling, Identification and Control of Friction System: Application to Clutch System Control and to Acyclisms Filtering by Sliding Control], PhD Thesis, Université Paris Sud-Paris XI, 2008.